

The Effect of Anvil Geometry and Welding Energy on Microstructures in Ultrasonic Spot Welds of AA6111-T4

R. JAHN, R. COOPER and D. WILKOSZ

The formation of ultrasonic spot welds of AA6111-T4 has been investigated using a single-transducer unidirectional wedge-reed welder. The evolution of weld microstructures and weld strength due to anvil cap geometry and welding energy was studied. The variations in lap-shear failure load and weld microstructures as a function of welding energy were only slightly influenced by the changes in the anvil cap geometry. Weld failure in lap-shear tensile tests occurs by interface fracture for low energy welds and by button formation for high energy welds. Initially, microwelds or weld islands several microns in diameter are generated presumably at asperities of the two pieces being joined. As the welding energy increases, the weld interface can change from a planar to a wavy morphology and the weld strength increases. Deformation wakes and bifurcation are ubiquitous in strong welds. Microporosity is observed at the periphery of growing weld islands and along the flow lines associated with the wavy deformation microstructures. Grain growth occurs inside the weld zone after isothermal annealing. However, the porous microstructure at the weld interface is not affected by isothermal annealing. Ultrasonic spot welding of AA6111-T4 aluminum was found to be insensitive to variations in anvil cap size and the knurl patterns investigated in this research.

DOI: 10.1007/s11661-006-9087-0

© The Minerals, Metals & Materials Society and ASM International 2007

I. INTRODUCTION

ULTRASONIC metal spot welding (USW) uses cyclic vibration to form a lap joint between two metal sheets under static clamping pressure. The direction of vibration is in the plane of weld interface as compared to that typically used for ultrasonic joining of thermoplastic polymers. The vibration frequency for the majority of metal welders is typically 20 kHz and above, although some commercial welders are available to operate at lower frequencies. The electrical energy required for welding two AA6111-T4 coupons of 0.9-mm thickness by single-transducer wedge-reed welders is approximately 800 J. This is one to two orders of magnitude lower than the 50 to 100 kJ required for resistance spot welding. Additionally, in contrast to fusion welding technologies, USW does not produce a heat-affected zone that can degrade the strength of the metals being joined.^[1]

The mechanism by which ultrasonic welding produces strong welds is not well understood, despite past research efforts in microelectronics^[2,3,4] and multilayer prototype components.^[5] Many published hypotheses are based on contact mechanics^[6,7,8] and incorporate the associated frictional heating. Although contact mechanics models sufficiently approximate thermomechanical interactions at the weld interface, they ignore the nonlinear stress waves excited by cyclic vibrations and

dynamic instability^[9,10] in solid materials. Consequently, it is difficult to explain or predict microstructural changes that USW produces in welds between relatively thick sheets. Recently, some experimental evidence of material changes induced by high intensity ultrasonic vibration at 20 kHz in steel^[11] has been reported using scanning electron microscopy (SEM). Nanofeatures of unspecified nature were observed to nucleate at grain boundaries, but not inside the grains. The dominant microstructural mechanism for strong welds is likely to depend on the domain of welding parameters, which vary widely among applications and alloy thicknesses.

The USW is strongly affected by the design of the gripping surface of the sonotrode tip in single-transducer wedge-reed welders. It is likely that the contact geometry of the anvil cap, such as the contact area and knurl pattern, could also influence the performance of USW. Additionally, the weld microstructures vary with the input welding energy. These effects of anvil contact geometry and welding energy have not been systematically investigated and will be described in this article.

II. EXPERIMENTAL PROCEDURE

Sheets of AA6111-T4 alloy were obtained from Alcan in as-rolled condition. These sheets were sheared into weld coupons of 101.6 mm × 25.4 mm × 0.9 mm. The coupon length dimension was parallel to the rolling direction. The average surface roughness across the rolling direction is 1.0- μ m Ra. There is no additional processing to modify either surface roughness or surface oxide. In order to ensure an identical amount of

R. JAHN, Technical Specialist and R. COOPER, and D. WILKOSZ, Research Engineers are with Ford Research and Advanced Engineering, Ford Motor Company, Dearborn, MI 48121, USA. Contact e-mail: rjahn1@ford.com

Manuscript submitted May 19, 2006.

Article published online April 6, 2007.

stamping lubricant on each surface prior to ultrasonic welding, the residual stamping lubricant on the surface of aluminum coupons was removed by immersion in hexane. Stamping lubricant was then reapplied to the coupon surface at 1.0 g/m^2 density by controlled spray. This lubrication step was done to simulate the production environment where USW would occur immediately after stamping.

The coupons were overlapped for 25.4 mm along the length direction, forming an overlap area of $25.4 \times 25.4 \text{ mm}^2$ for lap welding. The welds were located at the center of the overlap area. The vibration direction of the welding operation was perpendicular to the length dimension of the coupon.

A wedge-reed-type Sonobond (PA, USA) welder, model MH2014D, configured with a customized power controller was used for welding. The same sonotrode tip (ID 124) was used in all experiments. The ridges of the tip knurl pattern were oriented perpendicular to the vibration direction. A hollow anvil post was designed and installed on the welder. It contains a socket at the end of the post to receive the taper-fit anvil cap, similar to the hollow reed for sonotrode tips. Three different anvil caps, shown in Figure 1 and described in Table I, were used in the experiments. The effective contact size at the weldment is determined by the smaller of the sonotrode tip and anvil cap in the experiment.

The grids of caps 139 and CT-4 were oriented 45 deg to the vibration direction. The geometry of cap 128 is identical to that of tip 124. Its ridges were oriented perpendicular to the vibration direction during welding, the same as the sonotrode tip. Due to the geometric symmetry of tip 124 and cap 128, an angular offset of 1.0 to 3.0 deg about the reed axis was incorporated into the mounting alignment of the tip and cap, to prevent interlocking during vibration.

All welding experiments were conducted at 2500 W, impedance setting 8, and line pressure 100 psi. Energy loss in the welder and in the transmission through the weldment coupon is not taken into account.

Tensile tests of the welds were conducted to measure the lap-shear failure load with an Instron 55R1125 (Norwood, MA, USA) load frame equipped with a 5 kN load cell at a constant displacement rate of 10 mm/min, at room temperature, and in ambient atmosphere. The samples were loaded along the length direction of the joined coupon pairs. Five samples for each welding condition were tested.

Cross-sectional samples for optical microscopy and SEM were prepared from the welded lap joint coupons by sectioning with a low speed diamond saw through the weld region either parallel or perpendicular to the vibration direction of ultrasonic welding. The section plane is always perpendicular to the broadfaces of the weld coupons. Sectioned samples were mounted using

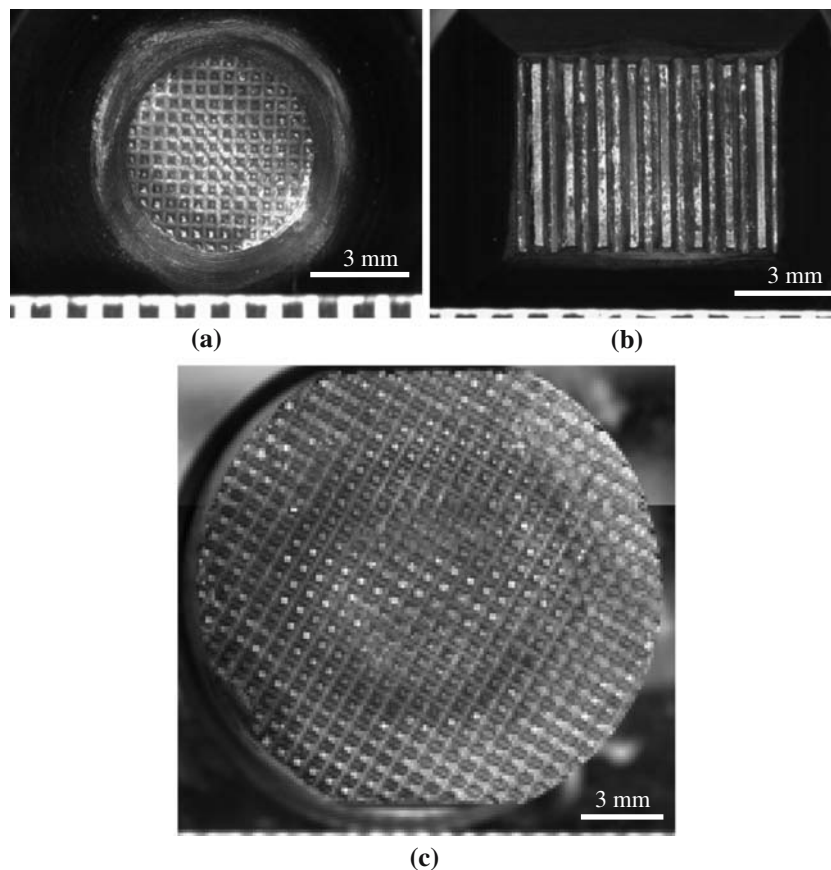


Fig. 1—(a) Anvil cap (ID 139) of smaller size. (b) Anvil cap (ID 128) of identical size to that of the sonotrode tip. (c) Anvil cap (ID CT-4) of larger size.

Table I. Geometric Attributes of Anvil Caps

Cap ID	Size (mm ²)	Knurl
139	19.6	truncated pyramid, 60 deg, depth 0.15 mm, spacing 0.38 mm
128	42.0	trapezoid, 75 deg, depth 0.38 mm, spacing 0.89 mm
CT-4	283.5	truncated pyramid, 95 deg, depth 0.26 mm, spacing 0.80 mm

two-component epoxy resin to minimize heating of the weld microstructure. The mounted samples were polished with SiC paper to 600 ANSI grit, followed by alumina paste to 0.3 μm , and finally by vibratory polishing in colloidal silica of 0.05 μm with a Buehler Vibromet I polisher (IL, USA).

Polished weld samples were etched by either of two etchant solutions (in vol pct): (1) 2 pct HF, 8 pct H₂SO₄, the balance of H₂O; or (2) 2.5 pct HBF₄, the balance of H₂O. The etching was conducted at a room temperature of about 25 °C. The samples were cleaned by immersion in an aqueous ultrasonic cleaning bath to minimize subsequent oozing of residual etchant out of the crevices at the weld periphery and in welds produced by low welding energies (short welding durations).

Isothermal annealing of sectioned welds was conducted at 550 °C for up to 25 minutes followed by a quench in water at 25 °C.

All microscopy images to be described in Section III are arranged such that the sonotrode tip side is at the upper side and the anvil cap side at the lower side, unless otherwise noted. The plane of the image is the section plane in cross-sectional weld samples. The weld interface, not necessarily planar, intersects the image plane at an approximately perpendicular direction. All weld images of low magnification are shown with the coupon region outside the weld zone that retains its original thickness of 0.9 mm.

A Nikon EpiPhot microscope (Kanagawa, Japan) was used for optical microscopy. Bright-field, grayscale imaging and differential interference contrast (DIC) imaging techniques^[12] for highlighting microstructural features were used. The SEM was conducted using a JEOL*

*JEOL is a trademark of Japan Electron Optics Ltd., Tokyo.

840A scanning electron microscope.

III. RESULTS

A. Attributes of Weld Development

1. Lap-shear strength

A plot of the lap-shear failure load of the weld as a function of the input welding energy is shown in Figure 2 for the three different anvil caps used in these experiments. Identical behaviors, in terms of the weld strength evolution, are exhibited by the three different anvil caps. Weld strength increases with increasing weld energy for input energies up to approximately 500 J. Weld strength becomes insensitive to higher input energies when the weld lap-shear strength reaches a plateau of 2.6 to 3.1 kN. In these lap-shear tests, the welds generally fracture along the weld interface for input energies of less than and equal to 400 J, while fracture occurs at the periphery of the weld (button pullout) for input energies of greater than 400 J.

There is a trend of increasing lap-shear failure load with increasing cap size in the plateau strength stage. For example, the average lap-shear failure load for welds with cap CT-4 is approximately 10 pct higher than that for welds with cap 139. It is believed that this phenomenon is attributable to the observed thinning of the weld joint as aluminum is extruded around the sonotrode tip and anvil cap.

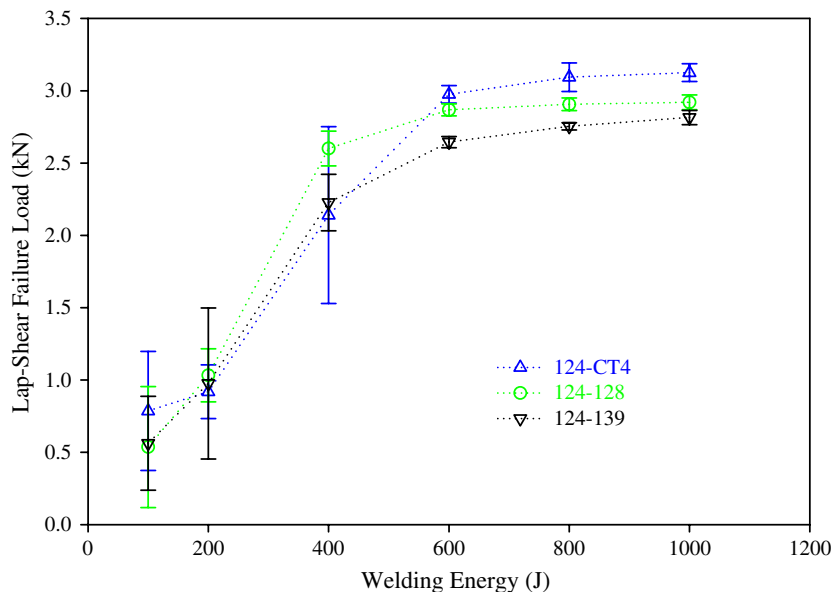


Fig. 2—Variation of lap-shear strength with welding energy for various anvil caps (ID 139, 128, and CT-4).

2. Measurement of weld features

A systematic method was developed to quantify various microstructural features in these ultrasonic welds using a commercial image analysis software package (ImagePro, MD, USA). The sectional weld size is

illustrated in Figure 3 as a function of welding energy. The sectional weld size is defined as the dimension of a weld measured in a section passing through the weld center and parallel to the vibration direction. Examples of weld size are shown in Figures 4(b) and 7.

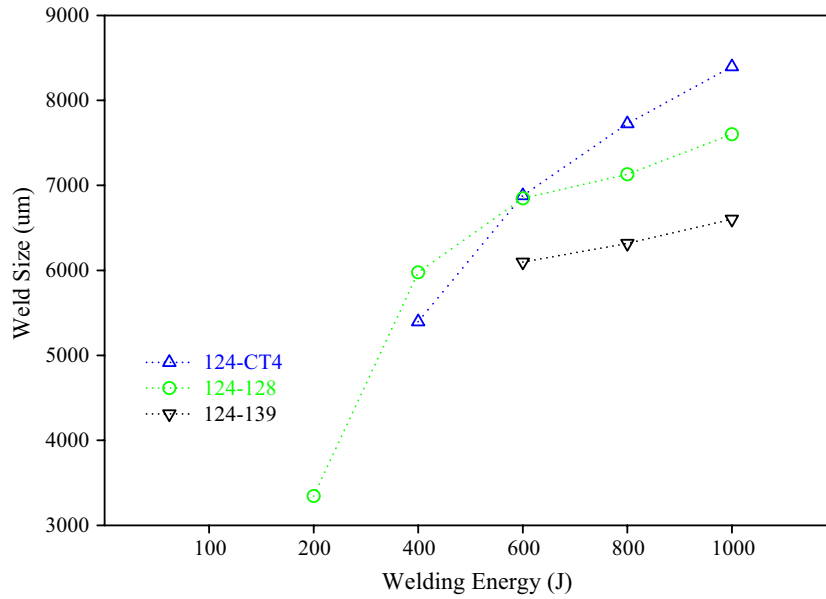


Fig. 3—Sectional weld size parallel to the vibration direction as a function of welding energy. Note that this sectional weld size can be different from the weld imprint size measured at the exterior surfaces. The sectional weld size measurement also differs from the button size measurement in lap-shear and peel tests.

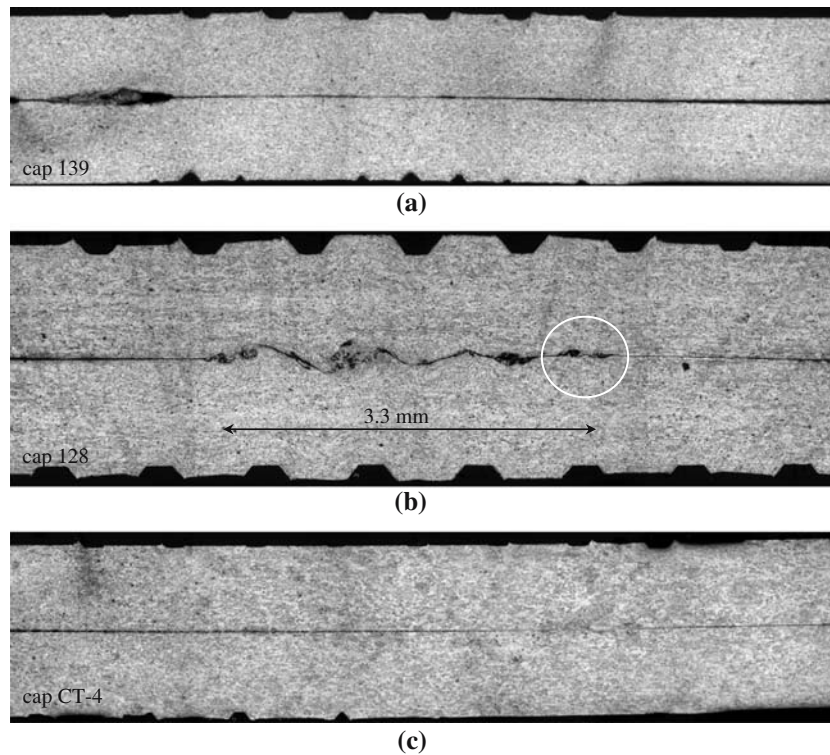


Fig. 4—(a) 200 J weld by anvil cap 139. Al sheet thickness outside weld imprint: 0.9 mm. (b) 200 J weld by anvil cap 128. Al sheet thickness outside weld imprint: 0.9 mm. (c) 200 J weld by anvil cap CT-4. Al sheet thickness outside weld imprint: 0.9 mm.

The weld size increases with the welding energy in all welds. For the same welding energy setting, weld size increases with the physical size of the anvil cap in the plateau strength stage. The weld size is always larger than the size of the smaller tool for asymmetric tip-cap configurations, *i.e.*, larger than cap 139 for tip 124-cap 139 and larger than tip 124 for tip 124-cap CT-4. The weld size in the plateau strength stage for the symmetric tip-cap arrangement is roughly the same as the physical size of the cap 128 (or tip 124), ranging from 6.8 to 7.6 mm at the section plane. A continuous weld zone emerges at lower welding energies in the symmetric configuration (tip 124-cap 128) when compared with other tip-cap configurations.

At low welding energies, it has been noted that aluminum has not been sufficiently deformed plastically to fill the valleys of the knurl patterns, as evidenced by the flat regions on the tip and cap side of the surfaces of these specimens (Figure 4). At 100 J, the maximum indentation depth into the weldment by either the tip or cap is less than 40 μm for welds with cap CT-4 and 40 to 80 μm for anvil caps 139 and 128. At 200 J, the maximum indentation depth becomes 80 μm for cap CT-4, 100 μm for cap 139, and 170 μm for anvil cap 128.

As mentioned in Section 1, measurements of weld thickness for weld energies greater than 600 J show that welds generated using anvil cap CT4 are 200- to 300- μm thicker compared to welds produced using anvil cap 139, possibly accounting for their higher lap-shear strength.

3. Formation of weld islands

Prior to etching the various as-polished cross sections of the welded specimens, the weld interfaces and the weld microstructures were not discernable. After

etching, the weld interface appears as a dark band in the low-magnification optical images, as shown in Figure 4 for the 200 J welds. Similar weld microstructures were observed for 100 J welds produced by these three different anvil caps. The wavy nature of the weld interface for anvil cap 128 is related to the pressure gradient during welding due to the grooves on the anvil cap and the sonotrode tip. The amount of waviness at the interface increases as a function of weld energy for all anvil caps but is more pronounced for anvil cap 128 at low welding energies. The contrast of the weld interface can be due to (1) preferential etching of heavily deformed material at the weld interface, (2) etching of interfaces between unbonded aluminum, or (3) preferential etching of aluminum adjacent to gaps or voids along the weld interface. The fact that the welds shown in Figure 4, as well as the ones produced by 100 J input energy, exhibit adequate strength for mechanical testing and sample preparation indicate some degree of bonding between the two aluminum coupons. Additionally, the lap-shear failure loads for the planar *vs* the wavy interface morphologies shown in Figure 4 are identical, indicating that both interface morphologies yield similar regions of bonded aluminum.

Detailed examination of the weld interface shown in Figure 4(b) showed complex deformation microstructures and very few discernable aluminum grain boundaries. One such area, circled in Figure 4(b), is shown in Figure 5(a). This region apparently shows two unwelded regions along the weld interface (two lower triangles annotated in this figure). Two deformation swirl structures comprised of deformation flow lines (strands) and elongated pores (10 to 30 μm) are observed adjacent to unwelded regions on the sonotrode tip side of the weld interface, as shown by arrows in Figure 5(a). We interpret the unwelded rim circumscribing the swirl

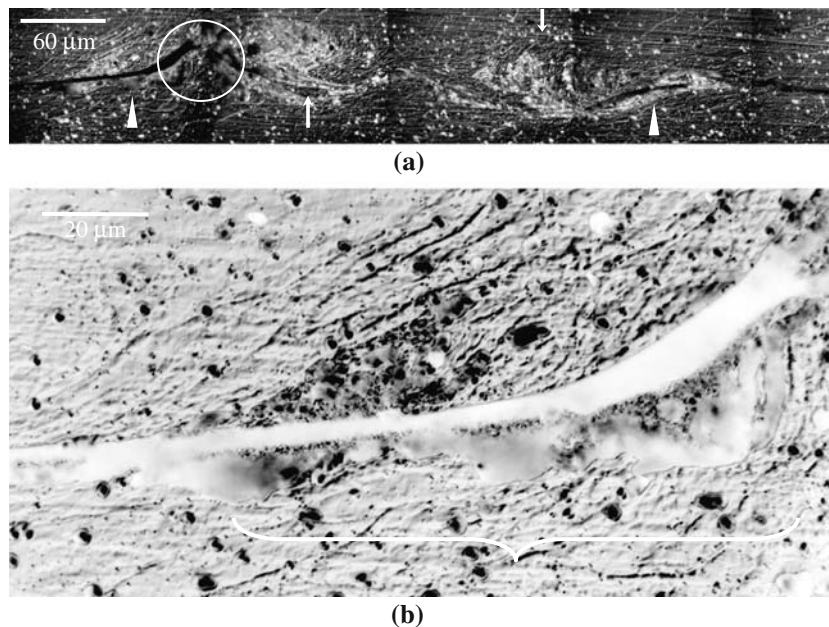


Fig. 5—(a) Weld island in a 200 J weld by cap 128, circle in Fig. 4(b). (b) Growth front (brace) of the weld island circled in (a). Negative of color DIC image converted into gray scale image.

structures to be the growth front of this weld island region, which is approximately $250\ \mu\text{m}$ in size. The size of these weld islands produced by cap 128 ranged between 150 to $500\ \mu\text{m}$ for the $200\ \text{J}$ welded sample and 150 to $400\ \mu\text{m}$ for the $100\ \text{J}$ welded sample. The length of the weld zone also showed an increase of size with welding energy, increasing from $2.5\ \text{mm}$ ($100\ \text{J}$) to $3.3\ \text{mm}$ ($200\ \text{J}$).

The left side of this weld island, circle in Figure 5(a), is shown in Figure 5(b) at a higher magnification. This region contains small round cavities and deformation flow marks similar to those observed in the swirl deformation region. The weld interface gap varies from $2\ \mu\text{m}$ far away from the weld island to $8\ \mu\text{m}$ in the immediate vicinity of the weld island. A region of very fine microporosity, less than a micrometer in diameter, is observed adjacent to the unwelded region on the anvil side of the weld interface (region denoted by the brace in Figure 5(b)). These small pores were easily distinguished by their purple color in the original color DIC image due to the difference of their depth from that of the section surface. Immediately below this region of microporosity are several subsurface cavities approximately 10 to $25\ \mu\text{m}$ in size, as evidenced by the out-of-focus regions in Figure 5(b) (area immediately above the brace). The microporosity on the anvil side of the weld interface and the flow lines or swirl patterns on the sonotrode tip side of the weld interface in this one particular area were not consistently seen in other areas of this particular weld or in welds made using higher energies.

In contrast to the welds produced by cap 128 at 100 and $200\ \text{J}$, the welds generated by caps 139 and CT-4 at 100 and $200\ \text{J}$ displayed planar interfaces, as illustrated in Figures 4(a) and (c). Aluminum grain boundaries are clearly visible adjacent to the weld interface, with no evidence of microporosity, cavities, or deformation flow lines, as shown in Figure 6. Small regions of aluminum, approximately 4 to $6\ \mu\text{m}$ in size for this weld produced by $100\ \text{J}$ input energy, are observed to bridge across the

weld interface of these etched specimens. It is not easy to retain these small weld islands near the section plane against preferential etching. These weld islands are visible as faint reflections from the remnant material deeper inside the weld interface. The remnant material of two weld islands on the left is connected to surface pits (in weld surface, not section surface) that were also preferentially etched. There is no evidence of frictional damage to the substrate in the nearby region other than some nonplanar nature of the mating surfaces. We presume that these weld islands are more resistant to chemical etching compared to the rest of the weld interface, because the deformation and recovery of the aluminum at certain locations along the weld interface produces new aluminum grains that bridge the original weld interface.

Despite the large differences in the extent of the weld islands and the weld interface morphology, welds produced by different anvil caps at the same energy setting have similar lap-shear weld strengths.

Welds produced using $400\ \text{J}$ input energy by all anvil caps exhibited nonplanar weld interfaces. These weld microstructures resemble those found in welds produced at higher energies in the plateau stage and will be described later. For welds by caps 139 and 128, the weldment material has almost fully filled the tip knurl. There is only partial filling into the tip knurl for welds by cap CT-4, as indicated by the presence of residual flat regions at the exterior contact surfaces.

4. Formation of deformation flow lines (wake features)

In the plateau strength stage of 600 to $800\ \text{J}$, welds by all three anvil caps show continuous weld zones fully extended from one end of the tip imprint to the opposite, as shown in Figure 7. Discrete weld islands are no longer present. The size of the weld zone closely agrees with the smaller of the two imprints from tip and cap contact.

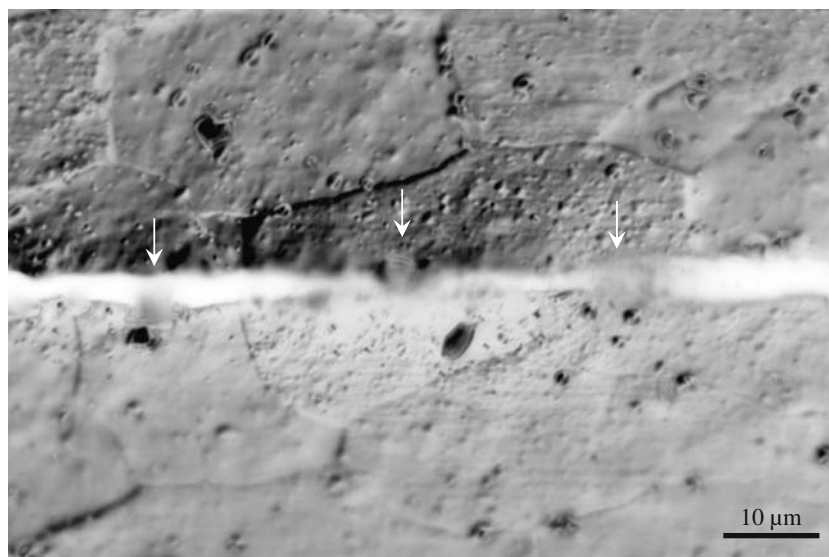


Fig. 6—Weld islands in a $100\ \text{J}$ weld by anvil cap CT-4 (focus on islands). Negative of DIC image.

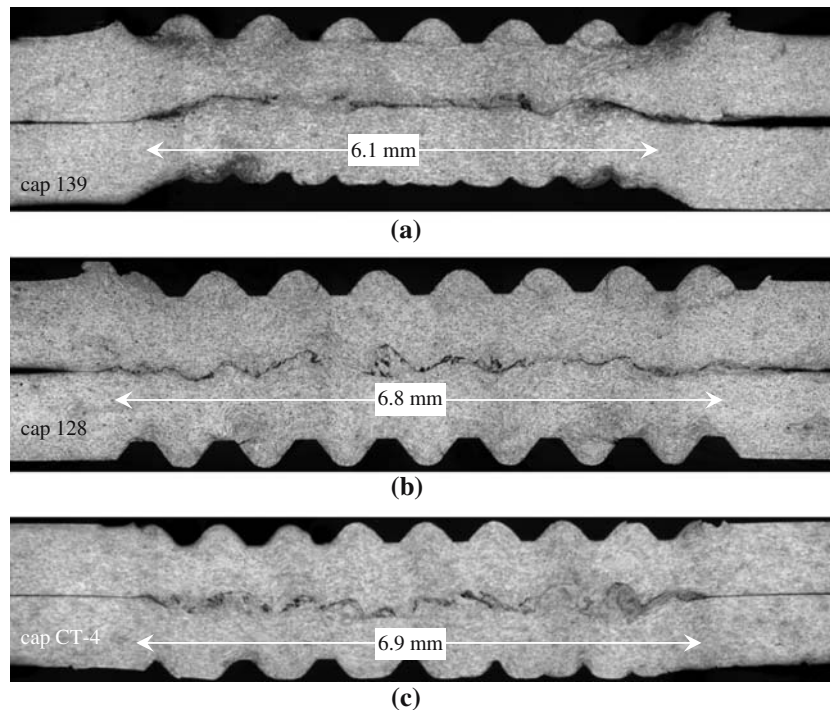


Fig. 7—(a) 600 J weld by anvil cap 139. Al sheet thickness outside weld imprint: 0.9 mm. (b) 600 J weld by anvil cap 128. Al sheet thickness outside weld imprint: 0.9 mm. (c) 600 J weld by anvil cap CT-4. Al sheet thickness outside weld imprint: 0.9 mm.

All welds show full penetration into the knurl patterns of both tip and cap. Surface extrusion at the rim of the weld imprint and distortion and gap opening at the weld periphery are found to increase as the welding energy increases in the plateau strength stage. The welds by the smallest cap 139 exhibit increasing indentation at the cap side as the welding energy increases.

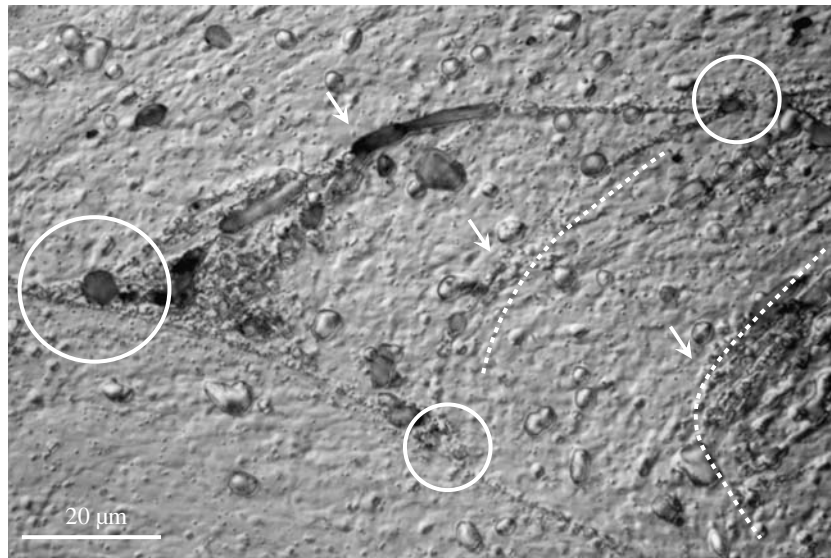
Wake features of deformation microstructures emerge sparsely during the growth stage and become abundant in welds of high welding energies at the plateau strength stage. Wake features in ultrasonic metal welds have been previously observed^[13,14] but not analyzed in sufficient detail. Consequently, no systematic description for wake morphology in ultrasonic welds exists in the literature. The generic term “wake” will be used in this article to describe microstructural features with any wake character in morphology. More definite descriptions, such as “vortex” or “ripple,” will be applied when appropriate for the feature morphology.

There are two types of wakes found in the welds. The coarse wakes are associated with interface morphology and can be easily discerned in low-magnification images. The amplitude of these coarse wakes is smallest for welds made by cap 139. In some welds, the interface can exhibit a sinusoidal pattern that bears resemblance to that of the tip knurl. It is tempting to identify a spatial correlation between the interface morphology and the tip knurl imprint. We have found that the spatial locations of “peaks” and “valleys” of the wavy interface relative to the tip knurl imprint pattern are transient and vary with the welding energy. A consistent (static) correlation does not exist between the spatial locations of the wake peaks and valleys and those of tip knurl imprint.

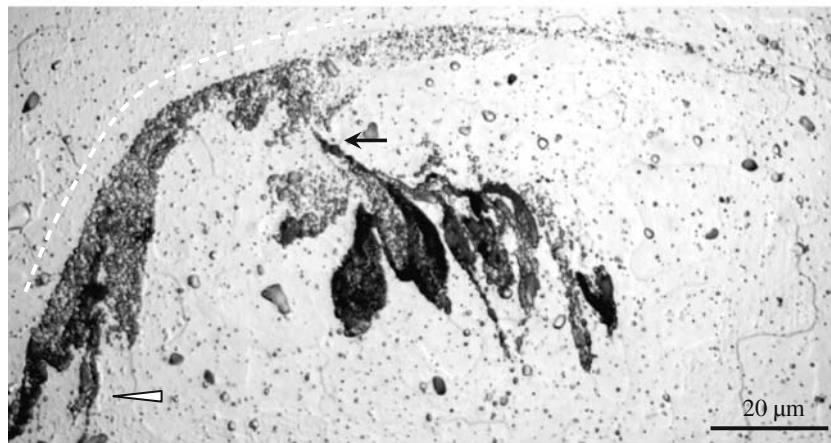
Finer deformation flow lines or secondary wake features (5 to 500 μm in extent) are observed to be associated with the coarser interface wakes. Their spatial orientations relative to one another are not random in sectional views, often forming patterns of ripple, splash, roll-up, and vortex shapes. Bifurcation, or branching, is observed when these flow lines join, and they rarely intersect by crossing over one another. An example of bifurcation is shown in Figure 8(a) for an AA6111 weld where bifurcation sites are indicated by circles. This field of view is part of a deformation wake. The primary weld interface is the line near the bottom of the image. Three deformation lines (arrows and dashed lines) are observed to bifurcate from the primary interface. Two of the deformation lines recombine in the field of view, off the primary interface, to form another bifurcation site.

A more complex feature of repetitive bifurcation is shown in Figure 8(b) in bright field and Figure 8(c) in negative DIC image. The bright area in Figure 8(c) corresponds to the dark area in Figure 8(b) due to preferential etching. The applied vibration is along the horizontal direction. The primary weld interface passes through this region as a porous band along the dashed line. A narrow strip of heavy deformation (arrow) branches off the primary interface. Several additional preferentially etched strands containing porous material emanate from this narrow strip at a distance from the primary weld interface. Notice that a low contrast area in the bright-field image can result from the low reflectivity of porous material in the etched area, as shown at the triangle site.

The plastic deformation in welds becomes excessive when the welding energies are further increased, as



(a)



(b)



(c)

Fig. 8—(a) Bifurcation (circles) of deformation flow lines at the weld interface. 600 J weld by cap 128. The line near the bottom is the primary weld interface. (b) Repetitive bifurcation along the weld interface. Bright-field image. (c) Same field as (b). Negative of DIC image. Focus on section surface.

shown in Figure 9 for welds of 1000 J. The excessive plastic deformation caused extrusion at the periphery of the tip imprint surfaces for welds by cap 139 and cap

128. It also led to a concomitant thickness reduction for welds by all three types of anvil caps. The average locations of the weld interface are no longer at the

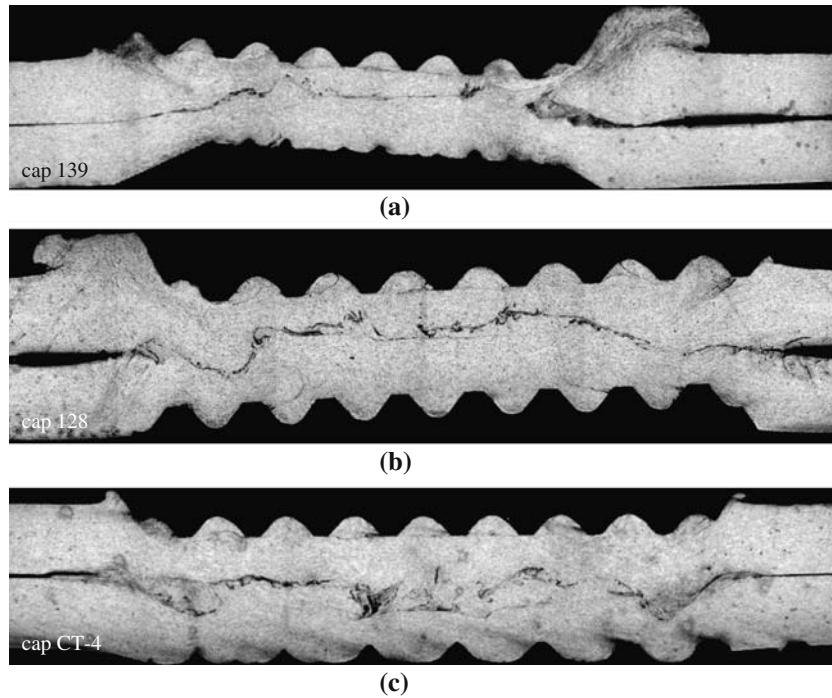


Fig. 9—(a) 1000 J weld by anvil cap 139. Al sheet thickness outside weld imprint: 0.9 mm. (b) 1000 J weld by anvil cap 128. Al sheet thickness outside weld imprint: 0.9 mm. (c) 1000 J weld by anvil cap CT-4. Al sheet thickness outside weld imprint: 0.9 mm.

middle of the weld thickness dimension. Instead, the interfaces have migrated toward the tip side of the exterior surfaces for welds made by cap 139 and cap 128.

5. Formation of microporosity near weld interface

Porosity is found not only in the vicinity of weld islands during the early stages of welding, as previously mentioned, but is also observed in welds of high welding energies. As an example, a pair of images of the same field of view, but with different focus settings, is shown in Figure 10 for a 1000 J weld by anvil cap CT-4. The spatial extent of submicron porosity increases substantially with welding energy. Multiple clusters of submicron porosity (arrows) are present near a large pit of $20\ \mu\text{m} \times 80\ \mu\text{m}$ in size in Figure 10(a). Material at a deeper depth inside the pit is not revealed due to the limited depth of focus.

When the focus is adjusted, a porous structure similar to cellular aluminum foam is observed in Figure 10(b). The pit is nearly completely filled with this foam structure. Similar porous microstructures are also partially revealed in other areas at this focus setting.

To better understand the porous microstructures at the USW interfaces observed by optical microscopy on etched cross-sectional specimens, weld specimens were examined in unetched condition *via* SEM using both secondary electron (SE) and backscattered electron (BE) imaging. An example of a 200 J weld by cap 128 is shown in Figure 11 in the as-polished condition. The matching half of this sectioned sample has been shown to contain weld islands, as documented in Figure 4(b) and 5. A region of material of $4.0\text{-}\mu\text{m}$ length (weld

island) is observed at the interface (circle in 11(a)), bridging the welding coupons. The interface gaps are about 0.5 and $0.1\ \mu\text{m}$ on either side of this weld island.

The image of the weld changes (Figure 11(b)) when the same area is imaged at 10 kV in the backscattered mode. Because BE images originate deeper beneath the surface, subsurface porosity not observed in the SE image is now visible as small ($< 0.5\text{-}\mu\text{m}$) dark circles in strands elongated parallel to the weld interface. A 1- to $3\text{-}\mu\text{m}$ surface layer of porous material exists at the tip side to the right of the weld island. Faint dark lines in the anvil side coupon in the SE image change into a strand of dark circles (porosity) in the BE image at 10 kV.

The BE images at 20 kV are qualitatively similar to that at 10 kV. The increased size of the electron interaction volume for 20-kV electrons results in the source of the BE signal for this image including material located further below the section surface. The porous microstructures observed at 10 kV are more evident at 20 kV. Additional faint dark strands nearly parallel to the weld interface also emerge in the anvil side coupon between the dark strand previously observed at 10 kV and the weld interface.

B. Formation of Deformation Flow Lines in Single Coupons Excited by Ultrasonic Strains

The spatial extent of vortex deformation patterns in lap-joint welds is limited to one side of the weld interface. The vortex patterns in lap-joint welds do not extend to the opposite exterior surface of the

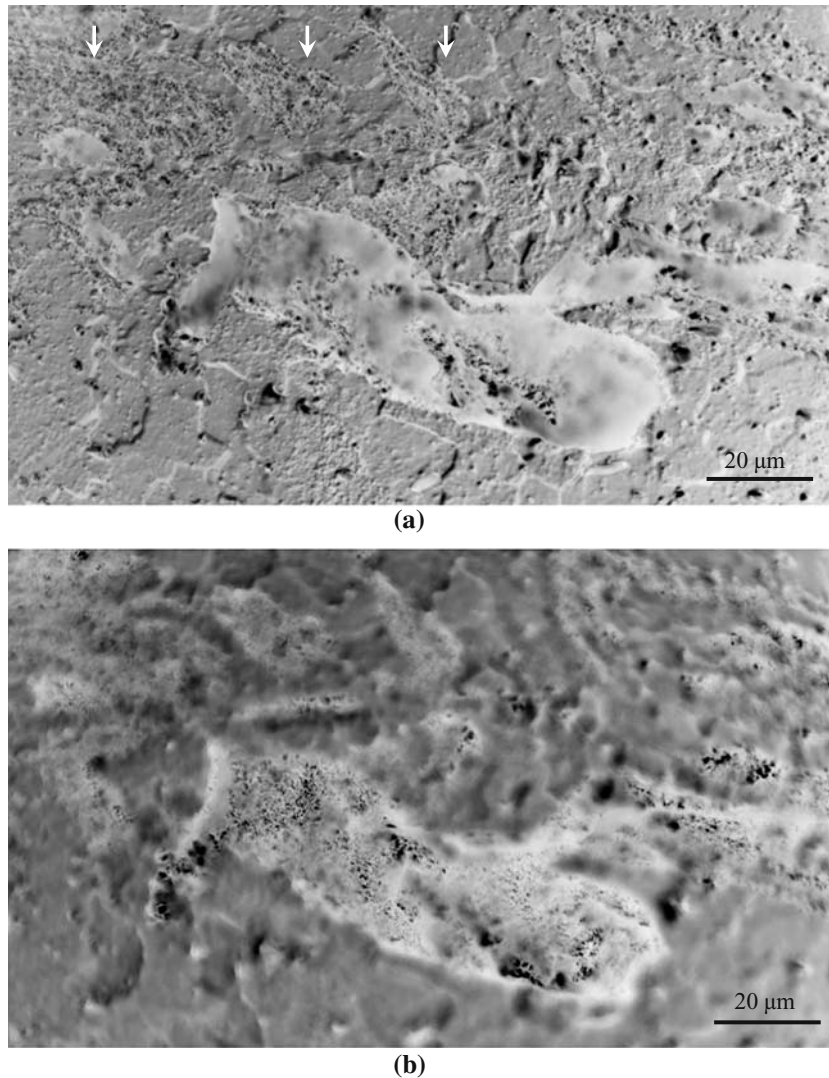


Fig. 10—(a) Porous regions in 1000 J weld by anvil cap CT-4. Focus on section surface. Negative of DIC image. (b) Porous material of sub-micron porosities (arrows) inside the large pit. Focus on selected depth in foamlike regions inside the large pit. Negative of DIC image.

weldment. In contrast, a different microstructure is found when the physical discontinuity (the starting weld interface) is eliminated during ultrasonic vibration. This is accomplished by using only one coupon between the sonotrode tip and anvil cap, as shown in Figure 12(a). The plastic deformation produces vortex-shaped deformation patterns extending from the top to the bottom of the sample. Grains of large aspect ratio, dispersed along the flow lines, dominate the deformation microstructure (Figure 12(b)). No evidence of microporosity was observed in these single coupon specimens.

C. Isothermal Annealing

Due to the elevated strain energy created by plastic deformation during welding, strain-induced boundary migration or exaggerated grain growth should take place when the welds are subjected to isothermal

annealing. An example is shown in Figure 13 for a weld subjected to isothermal annealing at 550 °C for 25 minutes. The sizes of grains inside the weld imprint zone have increased from 30 μm before welding to 100 to 200 μm after welding and annealing. The change of grain size outside the weld after annealing is negligible. Similar grain growth is observed when only a single coupon is subjected to ultrasonic vibration followed by isothermal annealing.

The porous microstructure along the weld interface also persists after isothermal annealing, shown as a low contrast wavy band near the weld center in Figure 13(a) and in more detail in Figure 13(b). Examination of this specimen *via* SEM (Figure 13(c) and (d)) shows in greater detail the porous microstructure after isothermal annealing at 550 °C for 25 minutes. A distinct line of contrast change is observed separating regions containing pores and deformation flow lines from the featureless large grain material.

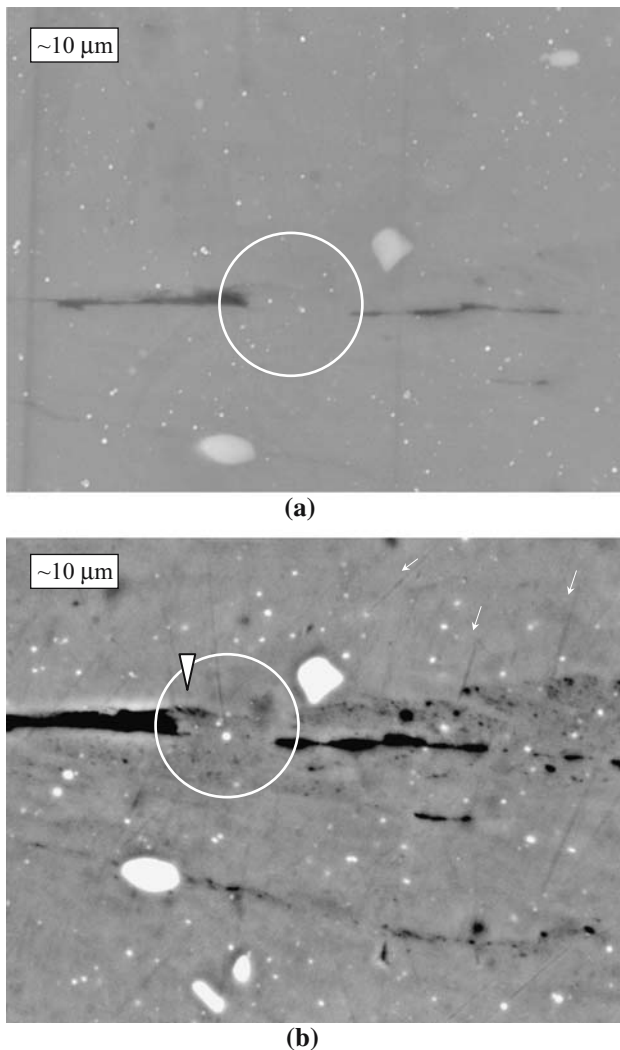


Fig. 11—(a) SEM image of the matching area in the opposite half weld for the weld island shown in Fig. 4(b). SE mode, 20 kV. Source of signal is mainly from the section surface. (b) SEM image of the same area as (a). BE image, 10 kV. Source of the majority BE signal is within $1\ \mu\text{m}$ of the section surface. Streaks of low signal intensity are present, nonuniform across the weld interface.

IV. DISCUSSION

Although the technique of ultrasonic welding metals has been known for over 50 years,^[13] the effects of many experimental parameters and a detailed microstructural model of the ultrasonic welding process remain unknown. In these experiments, the variation of the lap-shear failure load with increasing welding energy was found to be insensitive to the three different geometries of anvil caps (Figure 2). Nevertheless, different weld island sizes were produced in the early stage of welding ($< 200\ \text{J}$) by these anvil caps, as shown in Figure 6. The reason why variation of weld island sizes does not affect lap-shear failure loads is potentially related to the density of weld islands. A reliable measurement method for the density of weld islands by nondestructive ultrasonic inspection is currently in development. The most prominent difference in geometry for anvil cap 128

shown in Figure 1 and Table I is its smaller contact area at knurl ridges and hence initially larger contact stresses under the same nominal load. Somewhat surprisingly the different anvil cap geometries do affect the presence of the interface wake features. Coarse interface wakes are larger in welds made using anvil cap 128 compared to welds made using the other two cap geometries.

Initial formation of ultrasonic weld joints involves joining of small areas less than $10\ \mu\text{m}$. Past theoretical analyses have assumed elastic asperity contact^[6] and elasto-plastic asperity contact.^[4,5,8] These analyses are devised for frictional contact where the ultrasonic vibratory displacement vector remains uniform and parallel to the sliding surface. Localized frictional heating and plastic deformation at the contact points are critical factors in these models. The formation of weld islands or microwelds (Figure 6 and 11) observed at the earliest stages of ultrasonic welding in this study would appear to confirm this approach. The welds at this stage consist of weld islands dispersed among unwelded gaps in the weld zone, with no visible change in the grain structure in the adjoining aluminum. Although the exact nature of these weld islands remains controversial, recent transmission electron microscopy (TEM) characterization^[15] of ultrasonically welded aluminum alloys and Auger analysis^[16,17] of ultrasonically welded alumina to aluminum have identified chemical bonding across an oxide interface. In contrast, oxides were not reported in other TEM characterization efforts^[2,18] of ultrasonic aluminum welds. Detailed electron microprobe analysis carried out in this investigation failed to identify any oxides at the weld interface presumably due to their small sizes (10 to 20 nm).

Following the formation of weld islands, material flow lines or deformation wake structures are observed. The different geometries of the welding anvils clearly affect the amplitude of these wake features (Figures 4 and 7). Although no direct evidence exists, it is hypothesized that aluminum plastically flows around the harder weld islands during ultrasonic vibrations. The accumulation of irreversible plastic deformation in these regions and the concurrent heating by internal friction generates larger wake features as the welding time or energy increases. The deformation wakes have also been shown to be a complex physical motion of weld interface by monitoring the location of inert markers placed on one of the pieces of aluminum prior to welding. A significant observation occurring in conjunction with the formation of these wake features is the disappearance of well-defined grain boundaries adjacent to the wake features and the weld interface (Figures 5(b), Figure 8(b), and Figure 10(a)). Presumably, the plastic deformation that generates these wake features produces a significant density of pinned dislocations and dislocation cells. Some optical micrographs (not shown here) show rectangular subgrains in the vicinity of the weld interface. The TEM and orientation imaging microscopy (OIM) of similar ultrasonic welds^[19,20] have shown submicron and nano-grains in the vicinity of the weld interface. The isothermal annealing of the ultrasonic weld (Figure 13) unambiguously demonstrates

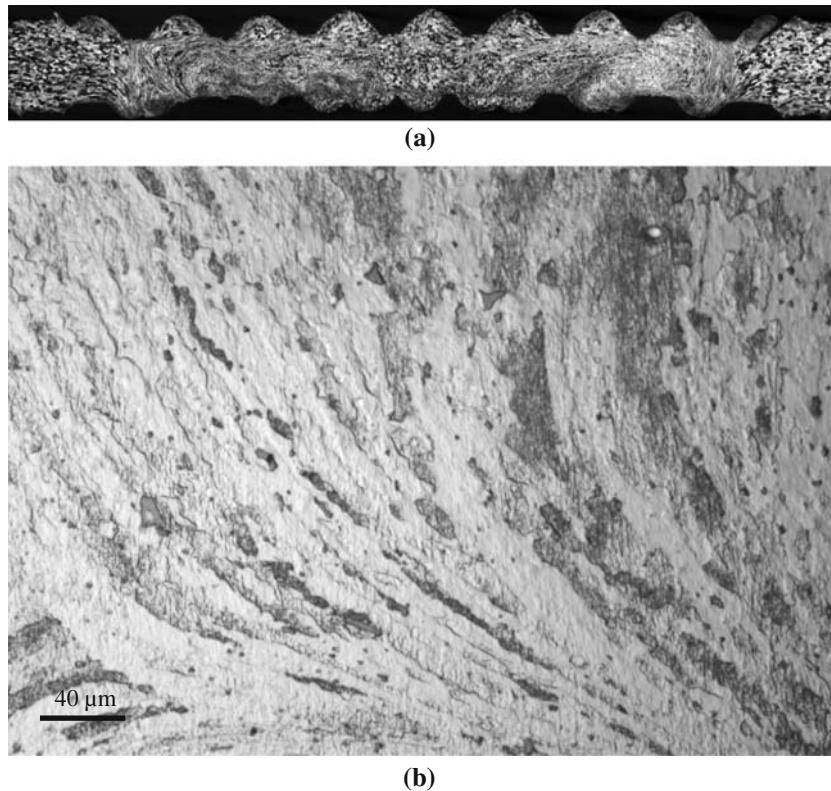


Fig. 12—(a) Vortex-shaped deformation patterns in the single coupon vibration experiment, in as-welded condition. (b) Dominant microstructure in ultrasonically vibrated single coupon.

exaggerated grain growth occurring in this highly deformed region.

The deformation wakes usually occur nearby, and are connected to, the weld interface, and their presence may be discontinuous and alternate on different sides of the weld interface. Their shape is complex in the cross-sectional view, sometimes appearing as parallel strands of very large aspect ratio (negligible thickness), sometimes as areas of equiaxed grains enveloped with deformation flow lines, and sometimes as vortices. In the absence of a weld interface, the deformation wakes become spatially extended and degenerate into a simple vortex shape between the exterior surfaces, as shown in Figure 12 for a single piece of metal subjected to identical ultrasonic vibration. An additional signature of deformation wakes in ultrasonic welds is the ubiquitous branching phenomenon, or bifurcation, as shown in Figure 8, among the deformation flow lines. The bifurcation phenomenon disappears when there is no weld interface, as shown in Figure 12 for a single coupon subjected to vibration. Interestingly, the observation of deformation wakes has not been mentioned in the literature of ultrasonic welding of thin-gage metals (foils, electronic wire splicing, *etc.*) where tips of different geometries and lower contact pressure are used.

Wake features of deformation microstructures have also been observed at the weld interface in metals joined by explosive welding.^[21–29] Explosive welding involves the initial melting and ejection of surface, followed by the formation of straight sections and vortices alternating along the wavy interface. Either crystalline phases or

isocahedral/amorphous phases^[30] can be found at the straight sections of bonding, and resolidified microstructures^[31,32,33] attributable to additional adiabatic heating and melting are identified at the vortex cores. In contrast, the wakes in ultrasonic welds occur in the absence of any microstructural evidence of melting at micrometer scale.

In addition to the wake features, regions of very fine microporosity are observed at higher welding energies adjacent to the weld interface. These regions of microporosity, which have an appearance resembling a foam structure, appear to replace larger gaps or voids at the weld interface observed for lower welding energies. The lack of any significant density of this microporosity in the single coupon, which was subjected to ultrasonic vibrations, shows that this microporosity is due to dispersion and refinement of the entrapped interfacial voids. Based on the result of SEM in Figure 11, we believe that the observed microporosity is not an artifact of etching and exists at lower levels even in lower energy welds.

V. CONCLUSIONS

The effect of anvil geometry on ultrasonic spot welds of AA6111-T4 0.9 mm alloy has been investigated using a unidirectional wedge-reed welder.

The development of lap-shear failure loads and weld microstructures exhibits similar behavior for the anvil caps investigated in the experiment. The weld strength

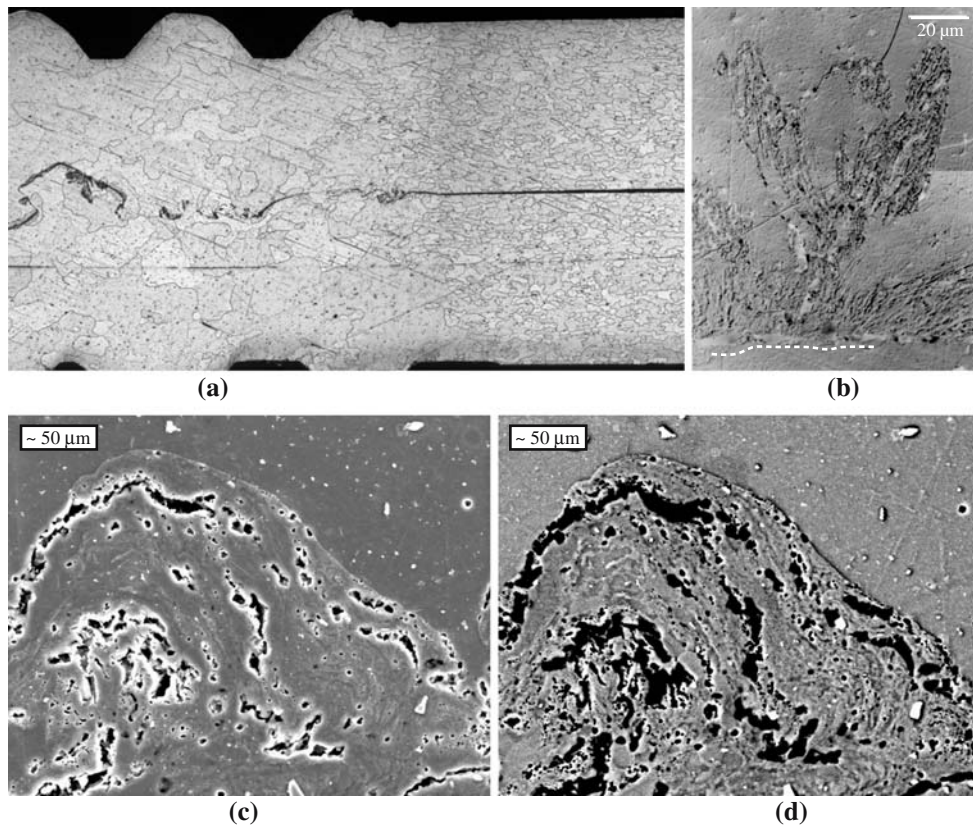


Fig. 13—(a) Grain growth inside the weld zone induced by isothermal annealing. (b) Porous microstructure at weld interface (dashed line) after isothermal annealing. Negative of DIC image. (c) Porous microstructure at weld interface after isothermal annealing, SE image. (d) Porous microstructure at weld interface after isothermal annealing, BE image.

increases with input energy up to 400 J during the growth stage. The weld strength reaches a plateau of 2.6 to 3.1 kN for weld energies greater than 600 J. Weld failure occurs in lap-shear tensile tests by interface fracture for low energy welds and by weld button pullout for higher energy welds.

The formation of weld islands dominates the stage where increasing weld energy results in higher lap-shear strengths. Continuous weld zones are found in the plateau strength stage where the weld interface changes from a planar to a wavy morphology. Concomitantly, deformation microstructures of wake shapes emerge during the growth stage and continue into the plateau strength stage. Microporosities are observed near weld islands and along the flow lines in deformation microstructures at the weld interface. Grain growth is observed inside the weld zone after isothermal annealing. However, the porous interfacial microstructure is not affected by isothermal annealing.

ACKNOWLEDGMENTS

The authors thank Mr. L. Reatherford for the effort in custom designed anvil post and Drs. S. Ward, W. Donlon, and J.E. Allison for in-depth discussion of the manuscript. This research is supported, in part, by

NIST ATP Cooperative Agreement No. 70NANB3H3015 of the United States of America.

REFERENCES

1. E. Lara-Curzio, L. Riester, and R. Jahn: Oak Ridge National Laboratory, Oak Ridge, TN, unpublished research, 2001.
2. J.E. Krzanowski: *IEEE Trans. Compon., Hybrids Manufact. Technol.*, 1990, vol. 13 (1), pp. 176–81.
3. N. Murdeshwar and J.E. Krzanowski: *Metall. Mater. Trans. A*, 1997, vol. 28A, pp. 2663–71.
4. Y.R. Jeng and J.H. Horng: *J. Tribol.*, 2001, vol. 123 (4), pp. 725–31.
5. Y. Gao and C. Doumanidis: *ASME J. Manufacturing Sci. Eng.*, 2002, vol. 124 (2), pp. 426–34.
6. E.A. Neppiras: *Ultrasonics*, 1965, pp. 128–35.
7. H.P.C. Daniels: *Ultrasonics*, 1965, pp. 190–96.
8. J.H. Horng: *ASME J. Tribol.*, 1998, vol. 121, pp. 82–89.
9. M.A. Zlatom and A.A. Kozhushko: *Sov. Phys.-Techn. Phys.*, 1982, vol. 27 (2), pp. 212–14.
10. J.D. Colvin, M. Legrand, B.A. Remington, G. Schurtz, and S.V. Weber: *J. Appl. Phys.*, 2003, vol. 93 (9), pp. 5287–5301.
11. Q. Han, C.L. Xu, G.R. Romanoski, D.T. Hoelzer, M.M. Menon, and R.P. Taleyarkhan: 2003 LDRD Seed Funding Project Report No. 3210–2038, Oak Ridge National Laboratory, Oak Ridge, TN, 2003.
12. M.R. Arnison, K.G. Larkin, C.J.R. Sheppard, N.I. Smith, and C.J. Cogswell: *J. Microsc.*, 2004, vol. 214 (1), pp. 7–12.
13. J.B. Jones and J.J. Powers: *Weld. J.*, 1956, pp. 761–66.
14. S.T.J. Yu and R. Jahn: *TMS Proc. Modeling the Performance of Engineering Structural Materials III*, TMS, Warrendale, PA, 2002, pp. 385–91.

15. A. Brodyanski, C. Born, and M. Kopnarski: *Appl. Surf. Sci.*, 2005, vol. 252, pp. 94–97.
16. J. Woltersdorf, E. Pippel, E. Roeder, G. Wagner, and J. Wagner: *Physica Status Solidi A*, 1995, vol. 150 (1), pp. 307–17.
17. T. Watanabe, A. Yanagisawa, and S. Sunaga: *Metall. Mater. Trans. A*, 2003, vol. 34A, pp. 1107–11.
18. J.E. Krzanowski and N. Murdeshwar: *J. Electron. Mater.*, 1990, vol. 19 (9), pp. 919–28.
19. E.A. Kenik and R. Jahn: *Microsc. Microanal.*, 2003, vol. 9, pp. 720–21.
20. S.M. Allameh, C. Mercer, D. Popoola, and W.O. Soboyejo: *J. Eng. Mater. Technol.*, 2005, vol. 127 (1), pp. 65–74.
21. A.A. Bahrani, T.J. Black, and B. Crossland: *Proc. R. Soc. Ser. A*, 1966, vol. 296 (1445), pp. 123–36.
22. J.N. Hunt: *Phil. Mag. (Ser. 8)*, 1968, vol. 17 (148), pp. 669–80.
23. G.R. Cowan, O.R. Bergmann, and A.H. Holtzman: *Metall. Trans.*, 1971, vol. 2, pp. 3145–55.
24. J.L. Robinson: *Phil. Mag.*, 1975, vol. 31 (3), pp. 587–97.
25. J.L. Robinson: *J. Appl. Phys.*, 1977, vol. 48 (6), pp. 2202–07.
26. S.V. Bazdenkov, V.F. Demichev, D.K. Morozov, and O.P. Pogutse: *Combust. Explos. Shock Waves*, 1985, vol. 21 (1), pp. 124–30.
27. V.M. Kornev and I.V. Yakovlev: *Combust. Explos. Shock Waves*, 1984, vol. 20 (2), pp. 204–07.
28. V.M. Kornev and I.V. Yakovlev: *Metall. Appl. Shock-Wave and High-Strain-Rate Phenomena*, 1986, pp. 961–67.
29. D. Jaramillo, V.A. Szecket, and O.T. Inal: *Mater. Sci. Eng.*, 1987, vol. 91 (7), pp. 217–22.
30. A. Chiba, M. Nishida, and Y. Morizono: *Mater. Sci. Forum*, 2004, vol. 465–466, pp. 465–74.
31. C.H. Oxford and P.E.J. Flewitt: *Metall. Trans. A*, 1977, vol. 8 (5), pp. 741–50.
32. S.K. Salwan: *India Weld. Res. Inst.*, 1987, vol. 8 (3), pp. 49–52.
33. F. Grignon, D. Benson, K.S. Vecchio, and M.A. Meyers: *Int. J. Impact Eng.*, 2004, vol. 30 (10), pp. 1333–51.